In-line Bragg magnifier based on V-shaped germanium crystals

Patrik Vagovič,[a,b]* Dušan Korytár,[b] Petr Mikulík,[c] Angelica Cecilia,[a] Claudio Ferrari,[d] Yang Yang,[a] Daniel Hänschke,[a] Elias Hamann,[a] Daniele Pelliccia,[e] Tamzin A. Lafford,[f] Michael Fiederle[g] and Tilo Baumbach[a]

[a]ANKA Light Source, Karlsruhe Institute of Technology, Karlsruhe, Germany, [b]Institute for Electrical Engineering, Slovak Academy of Sciences, Piešťany, Slovakia, [c]Faculty of Science, Masaryk University, Brno, Czech Republic, [d]Institute CNR-IMEM, Parma, Italy, [e]School of Physics, Monash University, ARC Centre of Excellence for Coherent X-ray Science, Vic 3800, Australia, [f]ESRF, Grenoble, France, and [g]FMF, Freiburg, Germany. E-mail: patrik.vagovic@kit.edu

In this work an X-ray imaging system based on a recently developed in-line two-dimensional Bragg magnifier composed of two monolithic V-shaped crystals made of dislocation-free germanium is presented. The channel-cut crystals were used in one-dimensional and in two-dimensional (crossed) configurations in imaging applications and allowed measurement of phase-contrast radiograms both in the edge-enhanced and in the holographic regimes. The measurement of the phase gradient in two orthogonal directions is demonstrated. The effective pixel size attained was 0.17 μm in the one-dimensional configuration and 0.5 μm in the two-dimensional setting, offering a twofold improvement in spatial resolution over devices based on silicon. These results show the potential for applying Bragg magnifiers to imaging soft matter at high resolution with reduced dose owing to the higher efficiency of Ge compared with Si.

1. Introduction

Hard X-ray imaging applications are of great interest, thanks to the large penetration depth of the photons and to the possibility of non-destructive investigation of the sample. Many full-field and scanning imaging systems have been developed which allow samples to be imaged with resolutions down to several tens of nanometers. These optics systems are based on, for example, Fresnel zone plates (FZP), compound refractive lenses (CRL) (Schroer *et al.*, 2005), Kirkpatrick–Baez (KB) mirrors (Hignette *et al.*, 2005; Mimura *et al.*, 2007), indirect detectors using luminiscent screen, optical microscope and CCD detectors (Koch *et al.*, 1998) and direct conversion detectors, for example Medipix.

The Bragg magnifier is a hard X-ray full-field imaging system which operates in the resolution range from about 300 nm up to 10 μm, filling the gap between KB, FZP, CRL microscopes and indirect detectors and providing high-contrast images free of scatter. Scattered signal decreases the image contrast but is rejected by the Bragg magnifier because the angular acceptance of its crystals is much smaller then the angular deviation of the scatter from the primary beam. The theoretical description of Bragg magnifiers was introduced by Spal (2001). A Bragg magnifier is composed of crystal optics which use the geometrical magnification provided by asymmetrically cut perfect crystals. Those crystals can be set both in one-dimensional (1D) and in two-dimensional (2D) configurations. 1D magnification can be obtained in the simplest way by using one asymmetrically cut crystal. It was first reported by Kohra (1972) where Cu $K_{\alpha 1}$ radiation was used. The magnification factor attained was 5.5. The scheme typically used to achieve 2D magnification consists of two crossed asymmetric crystals in σ-π configuration (Boetinger *et al.*, 1979; Stampanoni *et al.*, 2002; Schäfer & Köhler, 2003; Senin *et al.*, 2009), where the diffraction planes of the first and the second crystal are set perpendicular to one another. The 2D magnification can also be achieved by monolithic magnifiers where at least two successive sets of diffracting planes in one single-crystal block are magnifying the image in two orthogonal directions (Korytár *et al.*, 2003).

The present paper describes a recently developed in-line 2D Bragg magnifier microscope based on germanium channel-cut crystals. First results from experimental testing obtained at the European Synchrotron Radiation Facility (ESRF) BM05 beamline are presented. The configuration is similar to the one presented by Kobayashi *et al.* (2001) or by Kagoshima *et al.* (2000) but our magnifier consists of two channel-cut crystals instead of four independent crystals, and, instead of silicon
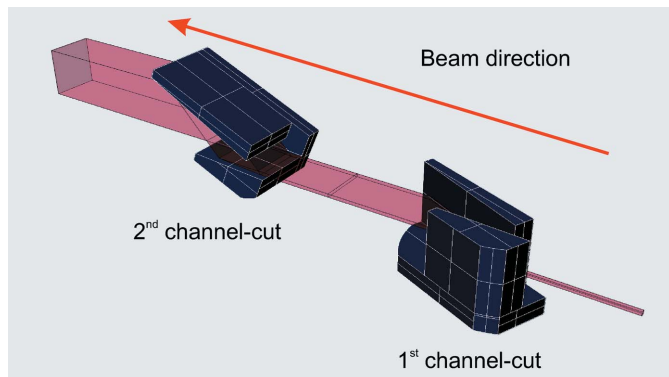
Figure 1
In-line 2D Bragg magnifier composed of two crossed V-shaped channel-cut crystals.

crystals, germanium crystals are used for the first time. A diagram of the in-line 2D Bragg magnifier composed of two crossed V-shaped channel-cut crystals is shown in Fig. 1.

2. Device description

The magnification by means of a single asymmetric crystal has the disadvantage that the output beam is diffracted into a direction which is not parallel to the input beam. A more appropriate solution would be to magnify the image in one direction by employing two diffractors, either polylithic or monolithic, in a non-dispersive $(+n, -n)$ crystal configuration. Basic coplanar crystals configurations have been described by DuMond (1937). By combining two such devices, *i.e.* one magnifying in one direction and another in the perpendicular direction (a non-coplanar crystal configuration known as σ-π), one would achieve an in-line arrangement which produces an output beam parallel to the input beam. For the 1D magnification, we used a monolithic channel-cut crystal with unequal asymmetries, a so-called V-shaped channel-cut crystal. By crossing two such V-shaped crystals in the σ-π configuration, where the diffracting planes of the channel-cut crystals are perpendicular, we achieved 2D magnification while still preserving the parallelism of the input and the output beams (Fig. 2). The big advantage of monolithic devices with respect to polylithic devices is their mechanical stability and significantly easier adjustment, since the relative orientation between the two sets of diffracting planes within the single crystal is precise and fixed. The diffracting properties of highly asymmetric V-shaped channel-cut crystals have been studied by Ferrari *et al.* (2011).

The magnification in one dimension of such a system is described by the magnification factor (m) which is, in the case of a channel-cut crystal, the product of the magnification factor of the first and the second diffractors [(m_1) and (m_2), respectively]. The Bragg magnifier uses high magnifications where the angle of the input beam is well below 1° with respect to the surface. For high magnifications, angular shifts owing to refraction are significant and need to be included to correct the magnification factor,
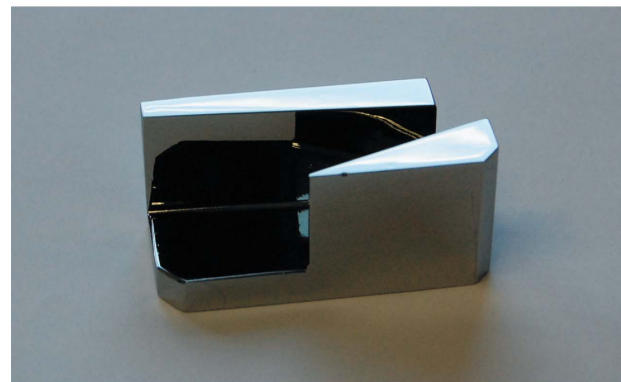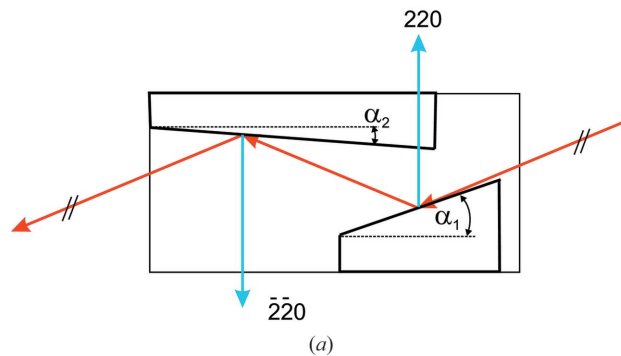

$$(a)$$

$$(b)$$

Figure 2
Geometry of the V-shaped channel-cut crystal (top); $\alpha_{1,2}$ are the asymmetry angles: $\alpha_1 = 19°$, $\alpha_2 = 4.28°$; photograph of the device (bottom). Crystals were prepared by Integra TDS in Slovakia.

$$m = m_1 m_2 = \frac{\sin(\theta_B + \delta_h^1 + \alpha_1)}{\sin(\theta_B + \delta_i^1 - \alpha_1)} \frac{\sin(\theta_B + \delta_h^2 + \alpha_2)}{\sin(\theta_B + \delta_i^2 - \alpha_2)}, \quad (1)$$

where θ_B is the Bragg angle, $\alpha_{1,2}$ are asymmetry angles (the inclination angles of the diffracting planes with respect to the surfaces) of the first and second diffractors of the channel-cut crystal, and $\delta_{i,h}^{1,2}$ are the refraction corrections for the input and output beams, for the first and second diffractors, respectively.

Germanium crystals have important advantages over silicon for the Bragg magnifier. Typically, the integrated reflectivity of Ge is two to three times larger than that of Si thanks to the larger structure factor of germanium. This leads to shorter acquisition times and thus a reduction in the dose deposited in the sample. To analyse the throughput of the Bragg magnifier one has to calculate the integral of the reflectivity coefficient over three coordinates, the vertical angle θ, the horizontal angle φ and the wavelength λ, and normalize it over the integrated angular volume Ω as follows,

$$\mathcal{T}_{\mathcal{R}} = \frac{\iiint\limits_{\Omega} \left[\prod_1^n R_i(\theta, \varphi, \lambda) \right] \mathrm{d}\theta \, \mathrm{d}\varphi \, \mathrm{d}\lambda}{\Omega}, \quad (2)$$

where $\Omega = \Delta\theta\Delta\varphi\Delta\lambda$, $R_i(\theta, \varphi, \lambda)$ are the reflectivity coefficients of the ith diffractor and n is the number of diffractors for the given magnifier. One can expect that the throughput for germanium magnifiers will be higher than for silicon magnifiers but the detailed study of the throughput will be the scope of our next work.

Table 1
Comparison of the main parameters of Bragg magnifiers for their optimum energy E_{opt}.

α is the asymmetry angle, δ_i is the refraction correction on the input, ω_i is the angular width of the input rocking curve, m_{opt} is the magnification at optimum energy (optimum magnification), and Δx_{res} is the resolution limit. (a) Kobayashi *et al.* (2001), (b) our Ge (220) magnifier, (c) Stampanoni *et al.* (2006), (d), (e) Schäfer & Köhler (2003), Modregger *et al.* (2006).

	Reflection				
	(a) Si (111)	(b) Ge (220)	(c) Si (220)	(d) Si (224)	(e) Si (004)
α (°)	7.53	19.00	9	42.52	33.17
E_{opt} (keV)	14.844	9.390	20.493	8.240	8.297
δ_i (arcsec)	176	389	129	322	319
ω_i (arcsec)	29	81	19	30	36
m_{opt}	87	95	143	184	171
Δx_{res} (µm)	0.60	0.34	0.67	1.03	0.86

In addition, as discussed by Spal (2001), the spatial resolution of Ge magnifiers is typically two times better than the spatial resolution of Si magnifiers. The spatial resolution can be estimated from the angular acceptance of the magnifier, which provides the maximum spatial frequency which is unattenuated. Because the angular acceptance varies with the magnification, the spatial resolution limit also depends on the magnification. The resolution limit (Δx_{res}) can be calculated by using the relation

$$\Delta x_{res} = 2\lambda/\omega_i, \qquad (3)$$

where λ is the wavelength of the X-radiation and ω_i is the angular acceptance of the magnifier (Spal, 2001). For Ge crystals the resolution limit is about 0.34 µm while for Si crystals it is above 0.6 µm. Fig. 3 shows a comparison of the resolution limits as a function of magnification for Si and Ge magnifiers. Table 1 shows basic parameters of silicon and germanium magnifiers.

The dielectric susceptibilities necessary for the calculation were used from the Stepanov X-ray server according to Lugovskaya & Stepanov (1991). Angular acceptances were calculated by applying the Rustichelli formula (Rustichelli, 1975).
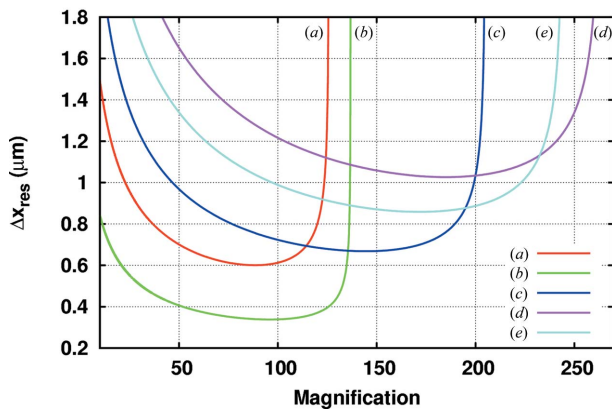
The resolution limit Δx_{res} can be considered as an intrinsic resolution limit of the Bragg magnifier. The final resolution of the complete system can be affected by other parameters, for example the penetration or the information depth and geometry used, source size and the sample-to-magnifier distance. The penetration depth z_e, or in the case of crystal optics it is better to speak about the information depth z_{inf}, is defined as the perpendicular distance from the surface when input radiation and output radiation is attenuated by the factor 1/e (Korytár *et al.*, 2008). The geometrical blur l_B of the pencil beam penetrating the crystal up to the information depth can be estimated as

$$l_B = z_{inf}\left[\cos(\alpha_i) + \frac{1}{m}\cos(\alpha_f)\right], \qquad (4)$$

where $\alpha_{i,f}$ are the input and output angles of the X-ray beam measured from the surface. In the case of a Ge (220) magnifier with asymmetry angle 19° at optimum energy 9.39 keV, the image blur l_B is comparable with the information depth $z_{inf} = 0.065$ µm and thus does not limit the resolution. The variation of the information depth is shown in Fig. 4.

A larger influence on resolution will be caused by the blurring caused by the finite source size and the sample-to-magnifier distance, so-called penumbral blurring, l_P, which is expressed as

$$l_P = sD_s/D, \qquad (5)$$

where s is the source size, D_s is the sample-to-detector distance and D is the source-to-sample distance. From the equation above it is clear that in the case of the bending-magnet source we can expect larger blurring in the horizontal direction because of its larger horizontal size.

Further blurring will be caused by Fresnel diffraction in the case of the coherent illumination. The point scatterer causes an interference of the scattered wave with the primary reference wave in the form of concentric fringes with radius $r_n =$
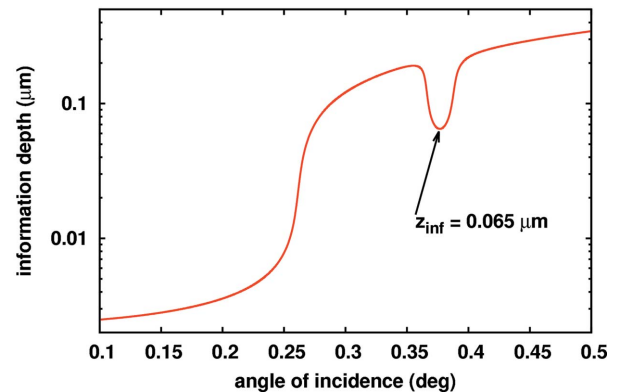

Figure 3
Comparison of existing Bragg magnifiers in terms of their resolution limit Δx_{res} calculated according to the equation (3). Each of these magnifiers works at different optimal energy E_{opt} (see Table 1). (a) Si (111) (Kobayashi *et al.*, 2001); (b) our Ge (220) magnifier; (c) Si (220) (Stampanoni *et al.*, 2006); (d) Si (224); (e) Si (004), $\alpha = 33.17°$ (Schäfer & Köhler, 2003; Modregger *et al.*, 2006).

Figure 4
Variation of the information depth as a function of input angle. The arrow shows the local minimum which corresponds to the center of the diffraction peak. Calculated at $E_{opt} = 9.39$ keV for Ge (220), $\alpha = 19°$.
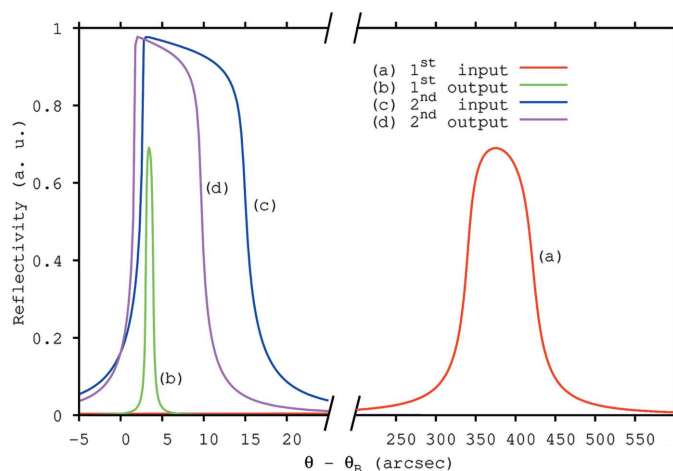
Figure 5
Intrinsic rocking curves of our V-shaped channel-cut crystal calculated at optimum energy of X-rays E_{opt} = 9.39 keV, where the input rocking curve (a) has maximum FWHM = 81 arcsec and the magnification of the first diffractor is 95. Rocking curves were calculated by applying a computational method for the two-beam case of dynamical diffraction theory (Huang & Dudley, 2003), and dielectric susceptibilities were used from the Stepanov X-ray server (Lugovskaya & Stepanov, 1991).

$(nD_s\lambda)^{1/2}$. Resolving two objects separated by some distance will then depend on the propagation distance used (the sample-to-detector distance). The Rayleigh or Sparrow resolution criterion can be used for that purpose. In the case where the higher diffraction orders from two objects are already overlapping at the detector position, it is impossible to resolve those two objects because the diffraction pattern is already recorded at that distance and one has to perform phase retrieval in order to obtain the spatial shape of the object.
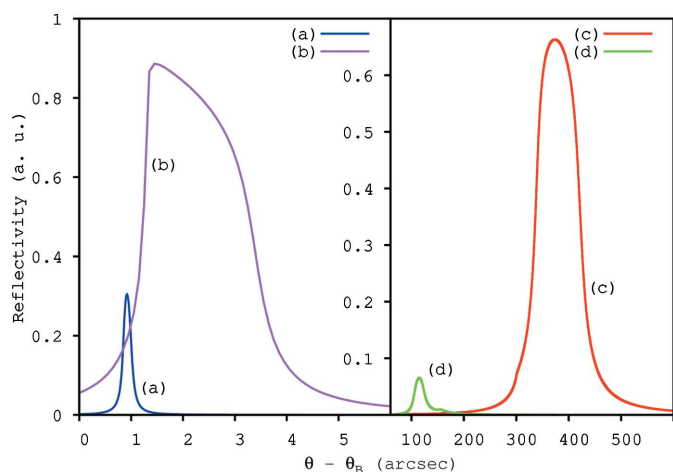

Figure 6
Suppression of higher-order harmonics with V-shaped channel-cut crystal for reflection (440) calculated at energy of X-rays E = 18.78 keV. (a) The output intrinsic rocking curve of the first diffractor, (440) reflection, E = 18.78 keV; (b) input rocking curve of the second diffractor, (440) reflection, E = 18.78 keV; (c) total input rocking curve, reflection (220), E = 9.39 keV (fundamental harmonic); (d) total input rocking curve, reflection (440), E = 18.78 keV (higher-order harmonic). Rocking curves were calculated by applying a computational method for the two-beam case of dynamical diffraction theory (Huang & Dudley, 2003), and dielectric susceptibilities were used from the Stepanov X-ray server (Lugovskaya & Stepanov, 1991).

The disadvantage of the channel-cut crystals is that it is impossible to select freely the asymmetry of the second diffractor, which limits the maximum magnification of such a system. In the case of germanium, the maximum attainable magnification is about 100. Higher asymmetry induces an increase of the refraction shift of the middle of the reflection domain. This can decrease the overlap of the intrinsic rocking curves with a consequent decrease of the system throughput. The detailed properties of asymmetric diffraction are very well explained by Authier (2004). In our case, we set the asymmetry of the second diffractor to completely overlap the output curve from the first diffractor with the input curve of the second diffractor. The intrinsic rocking curves of our V-shaped channel-cut system at 9.39 keV (the optimum energy of our system) are shown in Fig. 5.

In addition, by carefully selecting the asymmetry of the second diffractor, one can achieve suppression of higher-orders harmonics by overlapping the fundamental input rocking curve of the second diffractor with the output rocking curve of the first diffractor such that the corresponding curves for higher harmonics do not overlap (Fig. 6). In our case the higher-order harmonic passes through the system with about 10% transmission of the fundamental harmonic.

3. Experimental testing

We tested the performance of the Bragg magnifier at beamline BM05 at the ESRF in both 1D and the 2D configurations. The energies of the X-ray radiation were selected to be 8 keV and 9 keV and we demonstrated the imaging capabilities of our system on selected samples with very high spatial resolution reaching an effective pixel size of 0.17 µm. The X-ray energy 9 keV was chosen for the 1D case since it was close to the energy for optimum performance of the Bragg magnifier, and 8 keV was chosen for the tests of the 2D Bragg magnifier owing to limitations with the sample positioning system used.

In the 1D configuration, only one V-shaped crystal was used, to magnify the X-ray images in the vertical direction (Fig. 7a). The sample was a test pattern consisting of a boron–tungsten (B–W) fiber with a tungsten core surrounded by boron. The outer diameter of the fiber was 100 µm; the
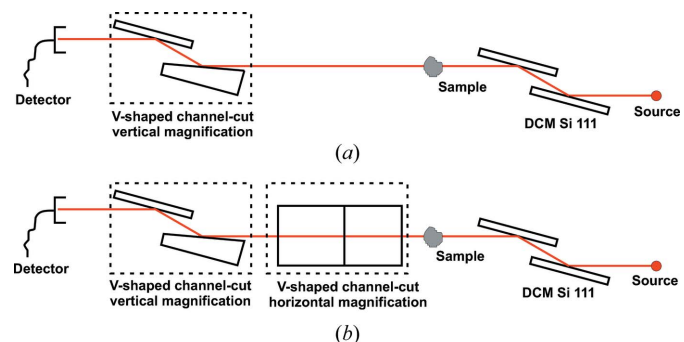

Figure 7
Experimental arrangement with (a) the 1D magnifier and (b) the 2D magnifier.

diameter of the tungsten core was 14 µm. The sample was placed 250 mm upstream of the 1D magnifier. The detector was a high-resolution system including a GADOX scintillator, optics and an ESRF FReLoN CCD camera. The effective pixel size of the detector was 7.5 µm. The energy was set to 9 keV using the beamline's Si 111 double-crystal mono-chromator (DCM).

The magnification obtained at 9 keV was 59 with an estimated effective pixel size of 0.17 µm. Fig. 8(a) shows an X-ray image of the B–W fiber recorded by the indirect detector. The high number of Fresnel oscillations beside the main diffraction peak [denoted by I_{max} in Fig. 8(b)] demonstrates the possibility of using a Bragg magnifier based on Ge crystals also for imaging in the holographic regime since access to the phase at the sample position is possible. The visibility of the oscillations is defined as

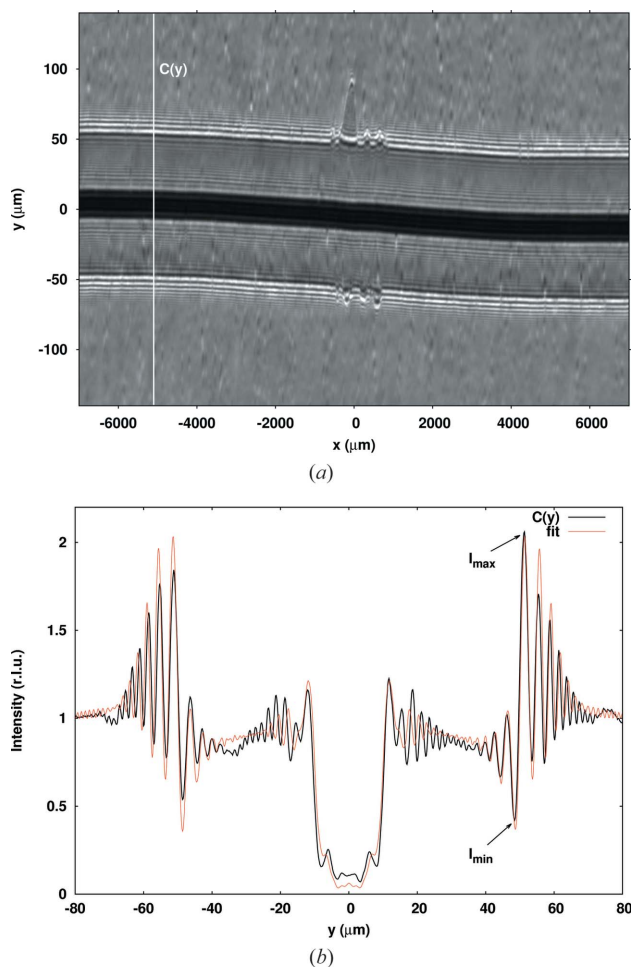$$V = \frac{I_{max} - I_{min}}{I_{max} + I_{min}}, \qquad (6)$$

Figure 8
Image of the B–W fiber obtained by the 1D magnifier (a) and the profile curve $C(y)$ (b) showing Fresnel oscillations along the cross section of the fiber. The gray (red online) curve is the numerical fit obtained by the simulation of Fresnel propagation of the complex projected thickness of the sample $T(y)$ onto the distance (250 mm from the sample) where the first diffractor is located. I_{max} and I_{min} indicate the maximum and minimum intensity of the main diffraction peak.
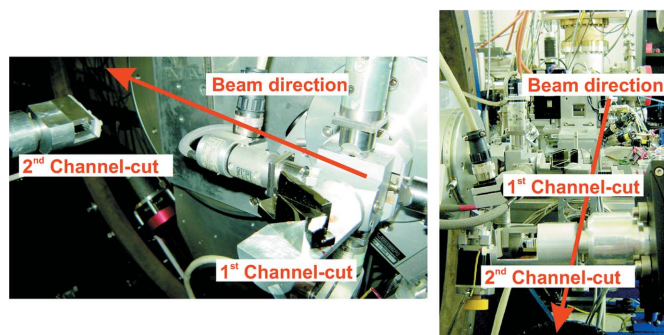

Figure 9
Experimental arrangement at beamline BM05 at the ESRF.

where I_{max} and I_{min} are, respectively, the maximum and minimum of the intensity oscillation (Fig. 8b). For the main diffraction peak, $V = 67\%$. In the case of Si magnifier(s), the higher-order Fresnel oscillations are strongly attenuated, as reported by Modregger *et al.* (2006). This is due to the fact that the input angular acceptance of the Ge crystals is larger than that of the Si crystals. The asymmetry of the oscillations on the left and right sides of the curve $C(y)$ is caused by the angular position of the input rocking curve which modulates the signal in the frequency domain like a low-pass frequency filter with a frequency cut-off corresponding to the width of the input rocking curve.

The numerical simulation (Fig. 8b), performed by Fresnel propagation of the transmission function of the model sample $T(y)$ onto the distance of 250 mm where the 1D Bragg magnifier was placed, shows very good agreement with the measured data although the function of the Bragg magnifier was not included in the simulation.

In the next step, we tested a 2D Bragg magnifier system by adding a second V-shaped crystal, magnifying in the horizontal plane, upstream of the vertical magnifier (Fig. 7b). The alignment of the system was rather fast, approximately half an hour, thanks to the in-line configuration. Photographs of the configuration are shown in Fig. 9. The detector was the same as that adopted for the 1D magnification case. By using the silicon 111 double-crystal monochromator, the energy was set to 8 keV, which resulted in a magnification of about 18 with an effective pixel size of 0.55 µm. In Fig. 10(a), an X-ray image of crossed B–W fibers is shown in the edge-enhancement regime. In this regime, only one Fresnel fringe across the boundaries of the objects is visible and thus we have access to the object boundaries. This is impossible to image in absorption contrast, where the detector is placed very close after the sample. Moving the detector further from the sample, the number of Fresnel oscillations increases. This regime is called the holographic regime where we have access to the phase of the object, whereas in the edge-enhancement regime the access to the phase is only partial. These regimes are described by Cloetens *et al.* (1999). The image of a human hair (Fig. 10b) was recorded in the holographic regime. The number of Fresnel oscillations indicates that the Bragg magnifier is preserving the coherence of the input beam. The arrow points to an interesting area in the image, where the deformation of
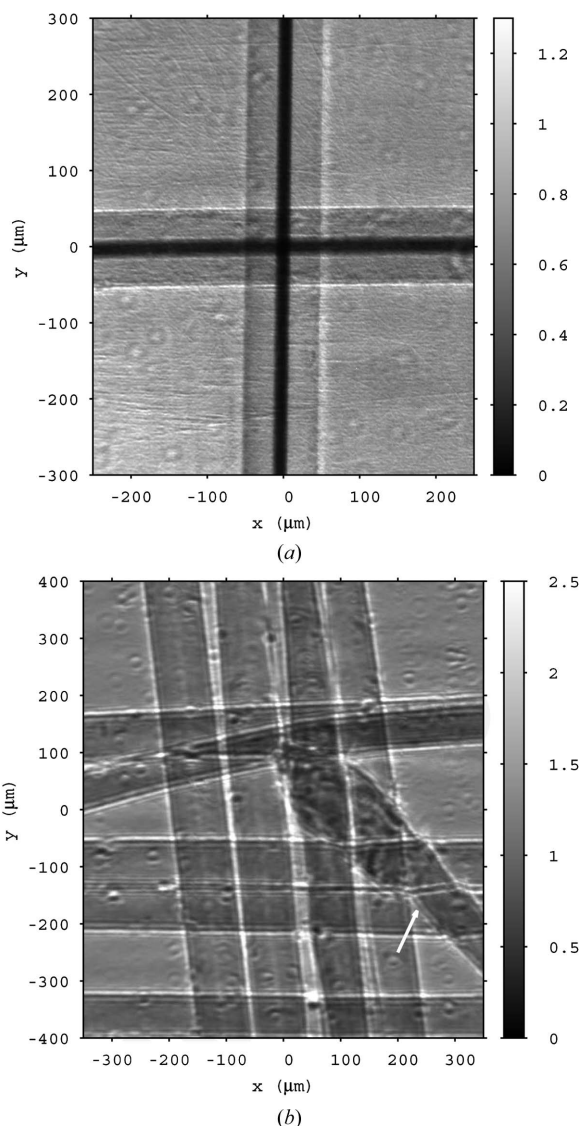
Figure 10
Image of crossed B–W fibers in the edge-enhancement regime (*a*) and the image of human hair in the holographic regime (*b*). The sample-to-magnifier distance was 150 mm in the case of the crossed fibers and 700 mm in the case of the hair.
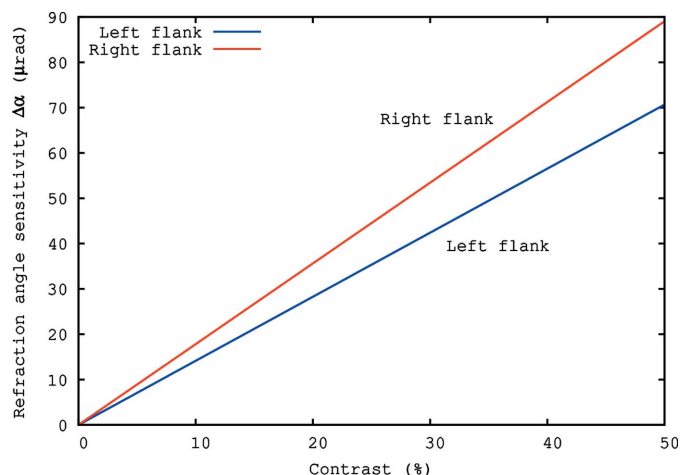

Figure 11
Variation of the refractive angle sensitivity as a function of the detectable intensity contrast for the V-shaped Ge crystal described above.

the wavefront caused by the sample is visible. Both images were recorded at the peak positions of the rocking curves of both V-shaped crystals.

Further, we tested the capabilities of the system for refraction contrast (phase gradient) measurements in two orthogonal directions, which was firstly proposed by Kagoshima *et al.* (2000). Similarly to the diffraction enhanced imaging (DEI) method (Chapman *et al.*, 1997), we can analyse angular deviations of the beam passing through the sample but in two orthogonal directions. These angular deviations are related to the phase of the wavefield passing through the sample *via* the first derivative as follows,

$$\Delta\alpha_x = -\frac{\lambda}{2\pi}\frac{\partial\varphi}{\partial x} \qquad \text{and} \qquad \Delta\alpha_y = -\frac{\lambda}{2\pi}\frac{\partial\varphi}{\partial y}, \qquad (7)$$

where λ is the wavelength of the radiation and φ is the phase of the wavefield passing through the sample. The extension of the standard DEI method to two-dimensional DEI was published by Modregger *et al.* (2007). Angular deviations lead to strong intensity modulations from which the refractive angle is usually estimated. The angular sensitivity in the case of a V-shaped channel-cut crystal can be estimated from the slope values of the flanks of the total input rocking curve. In the case of our V-shaped crystal, the variation of the refractive angle sensitivity with the variation of the contrast at the optimum energy 9.39 keV is shown in Fig. 11.

To test the method, we used the same model sample, the crossed B–W fibers, placed upstream of the magnifier. Images were recorded on the flanks and at the peak position of the first crystal, while keeping the second crystal at the peak position. The same set of images was then collected with the second crystal set on the flanks and at the peak, while keeping the first crystal at the peak position. Data were analysed separately for the horizontal and vertical phase gradients by the algorithm of Rigon (2007). The separate images for the horizontal and vertical components of the phase gradient are shown in Fig. 12.

4. Conclusions

The Bragg magnifier was successfully tested in the 1D and the 2D magnification cases at 8 keV and 9 keV, respectively. Phase-contrast radiograms were obtained in the edge-enhanced regime as well as in the holographic regime, showing the suitability of the Bragg magnifier for imaging samples of soft materials with very high resolution on a submicrometer scale with high contrast. Moreover, we demonstrated the use of our Bragg magnifier to the measurement of two orthogonal components of the refractive angle of the radiation refracted by the sample and thus we can apply our Bragg magnifier for measurement of two-dimensional phase gradients caused by samples. We reached an effective pixel size of 0.17 μm with a magnifier magnification of 59 but a further increase of the
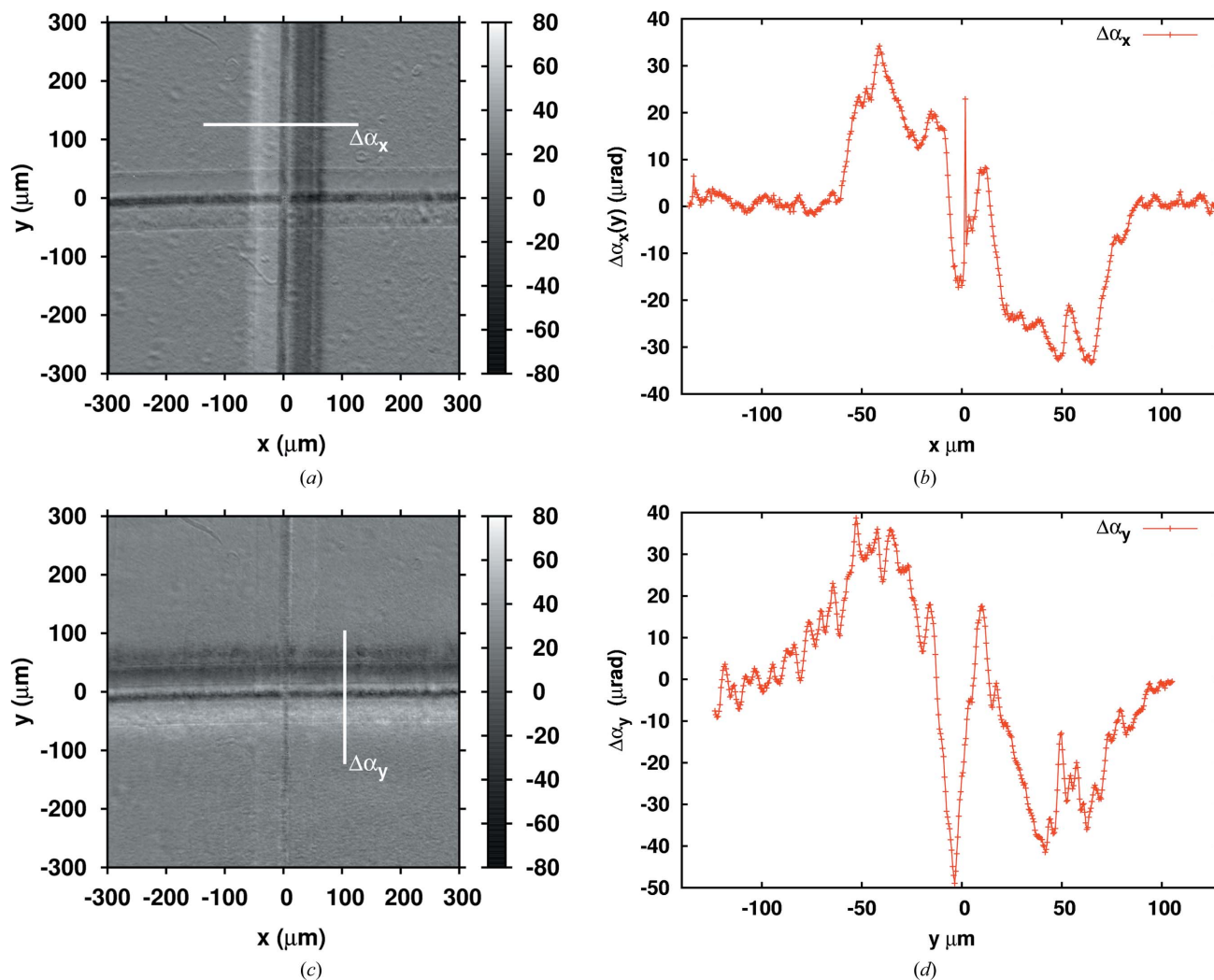
Figure 12
Refraction angle images of the crossed B–W fiber: horizontal $\Delta\alpha_x$ image (*a*) with its profile (*b*), vertical $\Delta\alpha_y$ image (*c*) with its profile (*d*). Refraction angle images were calculated by applying the algorithm of Rigon (2007). Gray scales are in microradians.

magnification up to about 80 is possible with this system. However, increase of the magnification causes image deformations which start to become significant because the surfaces of channel-cut crystals have lower optical quality than the surfaces of single planar crystals. This was also the reason why the magnifier was not tested at the optimal energy 9.39 keV. Technological improvements towards higher surface quality for channel-cut crystals will be the scope of further research. The spatial resolution of the system can be further improved by the proper combination of the detector pixel size, the magnification of the Bragg magnifier and usage of more parallel radiation provided by a smaller X-ray source like, for example, an undulator or by employing collimating optics placed before the sample.

References

Authier, A. (2004). *Dynamical Theory of X-ray Diffraction*. Oxford University Press.

Boettinger, W. J., Burdette, H. E. & Kuriyama, M. (1979). *Rev. Sci. Instrum.* **50**, 26.

Chapman, D., Thomlinson, W., Johnston, R. E., Washburn, D., Pisano, E., Gmür, N., Zhong, Z., Menk, R., Arfelli, F. & Sayers, D. (1997). *Phys. Med. Biol.* **42**, 2015–2025.

Cloetens, P., Ludwig, W., Baruchel, J., Guigay, J.-P., Pernot-Rejmánková, P., Salomé-Pateyron, M., Schlenker, M., Buffiére, J.-Y., Maire, E. & Peix, G. (1999). *J. Phys. D*, **32**, A145–A151.

DuMond, J. W. M. (1937). *Phys. Rev.* **52**, 872–883.

Ferrari, C., Germini, F., Korytár, D., Mikulík, P. & Peverini, L. (2011). *J. Appl. Cryst.* **44**, 353–358.

Hignette, O., Cloetens, P., Rostaing, G., Bernard, P. & Morawe, C. (2005). *Rev. Sci. Instrum.* **76**, 063709.

Huang, X. & Dudley, M. (2003). *Acta Cryst.* A**59**, 163–167.

Kagoshima, Y., Tsusaka, Y., Yokoyama, K., Takai, K., Takeda, S., Kobayashi, K., Kimura, H., Kimura, S. & Izumi, K. (2000). *AIP Conf. Proc.* **507**, 41–44.

Kobayashi, K., Izumi, K., Kimura, H., Kimura, S., Ibuki, T., Yokoyama, Y., Tsusaka, Y., Kagoshima, Y. & Matsui, J. (2001). *Appl. Phys. Lett.* **78**, 132–134.

Koch, A., Raven, C., Spanne, P. & Snigirev, A. (1998). *J. Opt. Soc. Am.* **15**, 1940–1951.

Kohra, K. (1972). *Proceedings of the Sixth International Conference on X-ray Optics and Microanalysis*, pp. 35–45.

Korytár, D., Ferrari, C., Mikulík, P., Germini, F., Vagovič, P. & Baumbach, T. (2008). *High Resolution 1D and 2D Crystal Optics Based on Asymmetric Diffractors.* In *Modern Developments in X-ray and Neutron Optics*, Vol. 137 of *Springer Series in Optical Sciences.* Berlin: Springer.

Korytár, D., Mikulík, P. C., Ferrari, J., Hrdý, J., Baumbach, T., Freund, A. & Kuběna, A. (2003). *J. Phys. D*, **36**, A65–A68.

Lugovskaya, O. M. & Stepanov, S. A. (1991). *Sov. Phys. Crystallogr.* **36**, 478–481.

Mimura, H., Yumoto, H., Matsuyama, S., Sano, Y., Yamamura, K., Mori, Y., Yabashi, M., Nishino, Y., Tamasaku, K., Ishikawa, T. & Yamauchi, K. (2007). *Appl. Phys. Lett.* **90**, 051903.

Modregger, P., Lübbert, D., Schäfer, P. & Köhler, R. (2006). *Phys. Rev. B*, **74**, 054107.

Modregger, P., Lübbert, D., Schäfer, P. & Köhler, R. (2007). *Appl. Phys. Lett.* **90**, 193501.

Rigon, L. (2007). *Appl. Phys. Lett.* **90**, 114102.

Rustichelli, F. (1975). *Philos. Mag.* **31**, 1.

Schäfer, P. & Köhler, R. (2003). *J. Phys. D*, **36**, A113–A117.

Schroer, C. G., Kurapova, O., Patommel, J., Boye, P., Feldkamp, J., II, B. L., Burghammer, M., Riekel, C., Vincze, F. & Küchler, M. (2005). *Appl. Phys. Lett.* **87**, 124103.

Senin, R. A., Buzmakov, A. V., Konovko, A. V., Smirnov, I. S., Geranin, A. S. & Asadchikov, V. E. (2009). *J. Phys. Conf. Ser.* **186**, 012035.

Spal, R. D. (2001). *Phys. Rev. Lett.* **14**, 3044–3047.

Stampanoni, M., Borchert, G. & Abela, R. (2006). *Radiat. Phys. Chem.* **75**, 1956–1961.

Stampanoni, G., Borchert, R., Abela, R. & Rüegsegger, P. (2002). *J. Appl. Phys.* **92**, 7630–7635.